High-Contrast Ultrafast Imaging of the Heart

Clement Papadacci, Mathieu Pernot, Mathieu Couade, Mathias Fink, and Mickael Tanter

***Abstract*—Noninvasive ultrafast imaging of intrinsic waves such as electromechanical waves or remotely induced shear waves in elastography imaging techniques for human cardiac applications remains challenging. In this paper, we propose ultrafast imaging of the heart with adapted sector size by coherently compounding diverging waves emitted from a standard transthoracic cardiac phased-array probe. As in ultrafast imaging with plane wave coherent compounding, diverging waves can be summed coherently to obtain high-quality images of the entire heart at high frame rate in a full field of view. To image the propagation of shear waves with a large SNR, the field of view can be adapted by changing the angular aperture of the transmitted wave. Backscattered echoes from successive circular wave acquisitions are coherently summed at every location in the image to improve the image quality while maintaining very high frame rates. The transmitted diverging waves, angular apertures, and subaperture sizes were tested in simulation, and ultrafast coherent compounding was implemented in a commercial scanner. The improvement of the imaging quality was quantified in phantoms and in one human heart, *in vivo*. Imaging shear wave propagation at 2500 frames/s using 5 diverging waves provided a large increase of the SNR of the tissue velocity estimates while maintaining a high frame rate. Finally, ultrafast imaging with 1 to 5 diverging waves was used to image the human heart at a frame rate of 4500 to 900 frames/s over an entire cardiac cycle. Spatial coherent compounding provided a strong improvement of the imaging quality, even with a small number of transmitted diverging waves and a high frame rate, which allows imaging of the propagation of electromechanical and shear waves with good image quality.**

I. Introduction

Echocardiography is the most common modality used to image the human heart in real time. Typical frame rates in two-dimensional echocardiography are in the range of 30 to 100 frames/s, allowing visualization of the heart motion and quantification of myocardial velocities and strains during the cardiac cycle [1], [2]. However, such frame rates are insufficient to track mechanical waves such as remotely induced shear waves [3]–[5] intrinsic shear waves [6] or electromechanical waves [7], [8] because of their high propagation speed in the myocardium (between 1 and 10 m/s).

In ultrasound imaging, the frame rate is limited by the number of transmitted ultrasound beams needed to construct an image. Many approaches have been developed to reduce the number of transmits, often at the cost of a lower spatial resolution or a reduced field of view. In 1977, an original approach based on an optical processing system to process the ultrasonics signals [9] was proposed by Bruneel *et al.* They obtained the first images of the cardiac muscle acquired at 5000 frames/s. However, the acousto-optics system required to implement this technique was too complex and this concept was abandoned. In 1984, Shattuck *et al.* [10] introduced a parallel beamforming system driving conventional imaging probes. In the conventional transmit focusing mode, the increase of the frame rate is typically achieved through the reduction of the number of beamformed lines in transmit, which either reduces the sector size or the line density of the image. Successive focused, ECG-gated acquisitions at high frame rates have also been proposed to maintain a large line density and sector [7], [8] but this approach cannot be used for real-time imaging of single heartbeats or shear wave imaging. The concept of ultrafast imaging using unfocused transmit waves [11]–[16] has been proposed to drastically reduce the number of transmits while maintaining the number of scan lines and the image size. The transmission of plane waves by linear transducer arrays has been successfully implemented on commercial scanners to image the propagation of remotely induced shear waves at frame rates up to 10 000 images/s in many organs of human subjects including the breast [17], liver [18], carotid artery [19], and cornea [20], and in the heart [3], [21], where it provides a noninvasive way to access the myocardial contractility [5]. Moreover, successive tilted plane-wave acquisitions can be combined either incoherently to improve transverse motion estimates [22] or coherently to increase the poor image quality obtained by using only one plane wave, both in terms of contrast and resolution. This technique, known as plane wave spatial compounding [23], has been shown to rapidly improve the image quality with the number of transmits without sacrificing the frame rate. With only 2 to 20 transmits, coherent spatial compound imaging can thus recreate a synthetic focus in transmit everywhere in the image, as is done in synthetic transmit aperture (STA) imaging techniques [24], but with high frame rate and large apertures for high SNR. STA was originally introduced in the field of ultrasonic imaging as a way to improve contrast and resolution of ultrasonic images by achieving dynamic focusing both in transmission and in reception. Driven by the need for higher frame rates, in particular for real-time 3-D imaging, sparse STA imaging techniques were then proposed [24]–[27]. These techniques can increase the frame rate by reducing the number of STA transmits at the cost of lower resolution, higher side lobe levels, and lower SNRs.

Using ultrafast imaging with coherent plane-wave compounding as well as sparse STA enables very-high-

Manuscript received July 17, 2013; accepted December 2, 2013. The research leading to these results has received funding from the European Research Council under the European Union's Seventh Framework Programme (FP/2007–2013)/ERC Grant Agreement number 311025.

C. Papadacci, M. Pernot, M. Fink, and M. Tanter are with the Institut Langevin, Ecole Superieure de Physique et Chimie Industrielles (ESPCI), CNRS UMR 7587, INSERM, U979, Paris, France, and with Université Paris Diderot-Paris 7, Paris, France (e-mail: papadacci.clement@gmail.com).

M. Couade is with SuperSonic Imagine (SSI), Aix-en-Provence, France.

DOI http://dx.doi.org/10.1109/TUFFC.2014.2909

frame-rate imaging (>1000 images/s) using only one to five transmits. In practical situations, the two techniques mainly differ in the diffraction of the transmitted beams, the amplitude of the plane wave being almost unaffected during wave propagation, which provides higher SNR at large depths. The geometry of the field of view also differs in the two techniques. For applications that require large fields of view, such as transthoracic cardiac imaging, the plane wave approach remains too limited. Transthoracic phased-array probes have small apertures that generate narrow plane waves which cannot cover the entire heart with a large sector.

Moreover, the coherent compound technique becomes rapidly inefficient when the imaging depths are large in comparison with the apertures, because the plane waves transmitted at different angles do not overlap in the region of interest. On the other hand, sparse STA allows imaging of a large sector, but at the cost of a lower SNR. In applications of ultrafast imaging such as shear wave imaging, very small tissue displacements are generated and high SNR is crucial to ensure the quality of the displacement estimation. However, in many cases, such as shear wave imaging or ultrafast Doppler imaging, it is not necessary to image the full sector. In these situations, a reduced field of view could be used to increase the SNR and improve the tissue and blood velocity estimation within the region of interest.

Based on our previous development of coherent compound plane waves, we propose to adapt this approach to ultrafast imaging with diverging waves to track the propagation of remotely induced and natural mechanical waves in the heart. The approach is similar to the method proposed by [26]–[29] in the framework of STA, by placing several virtual sources behind the probes to achieve real-time 3-D imaging. Hasegawa, Kanai and other groups [15] have also proposed a similar approach using diverging beams transmitted along several direction to cover the entire sector (15 transmits in [30]). Contrary to this approach, we propose here to transmit at very high frame rate, one or more diverging waves that insonify the entire field of view to achieve ultrafast imaging of the heart. In this paper, we focus on the practical implementation of this technique for 2-D ultrafast imaging of mechanical waves in the heart using a transthoracic phased array. First, we numerically investigate the positions of the virtual point sources in different situations to maximize the imaging quality and the SNR. Experiments are then performed in phantoms using a cardiac phased array to quantify the image quality increase in B-mode and shear waves velocity images

II. Simulation

A. Principles

In this section, the coherent summation of multiple diverging waves is performed analytically to investigate the synthetic focus achieved in transmit. In two dimensions, each transmitted circular wave is defined by the position of a virtual source located behind the probe.

The principle of coherent compounding with diverging waves is illustrated in Fig. 1. The choice of the position of virtual sources is crucial and can lead to very different results. For example, in synthetic aperture imaging techniques, the virtual sources usually coincide with the transducer elements and the diverging waves are successively generated by each element to restore a high-quality synthetic image [24]. However, at high frame rate, only a small number of diverging waves can be transmitted. In this case, if the virtual sources are superimposed onto probe elements, the total energy emitted is reduced and the large distance between sources will induce side lobes in the synthetic transmit field. To overcome this situation, the use of virtual sources placed behind the transducer was proposed [26].

The main problem is to determine where the virtual sources should be positioned to maximize the image quality while maintaining a very high frame rate?

Let's consider a virtual array of N point sources (from $-m$ to m) located behind the probe at positions $\underline{r_n}\begin{pmatrix} x_n \\ 0 \\ z_n \end{pmatrix}$ where z_n is kept constant for all the sources and $x_n = np$, where p is the pitch of the virtual array. If we apply the coherent summation of the acoustic fields generated by each diverging wave at a point $\underline{r_c}\begin{pmatrix} x_c \\ 0 \\ z_c \end{pmatrix}$ of space over the bandwidth (k_1, k_2), we can write the field $\Phi(\underline{r})$ as

$$\Phi(\underline{r}) = \int_{k_1}^{k_2} A(k) \sum_{n=-m}^{m} \frac{e^{jk|\underline{r}-\underline{r_n}|}}{|\underline{r}-\underline{r_n}|} \cdot e^{-jk|\underline{r_c}-\underline{r_n}|} \mathrm{d}k, \qquad (1)$$

where $e^{-jk|\underline{r_c}-\underline{r_n}|}$ is the phase correction needed to achieve the coherent summation at $\underline{r_c}$ and $A(k)$ is the amplitude. Eq. (1) can be simplified by considering the monochromatic far-field approximation at a focal distance F, near the central line ($x = 0$):

$$|\Phi(x)| \approx A(k) \frac{1}{F} \left| \frac{\sin(kp(x-x_c)N/2F)}{\sin(kp(x-x_c)/2F)} \right|, \qquad (2)$$

where $N = (2m+1)$ is the number of virtual sources (the complete derivation is given in the appendix).

From this expression, we can derive the dimension of the main lobe and the positions of the side lobes in the monochromatic case at the center frequency.

With $X = (x - x_c)$, zeros occur when

$$\frac{kp}{2F} NX = l\pi, \quad l \in \mathbb{Z} - \{Nk'; k' \in \mathbb{Z}\}, \qquad (3)$$

or, in other terms,

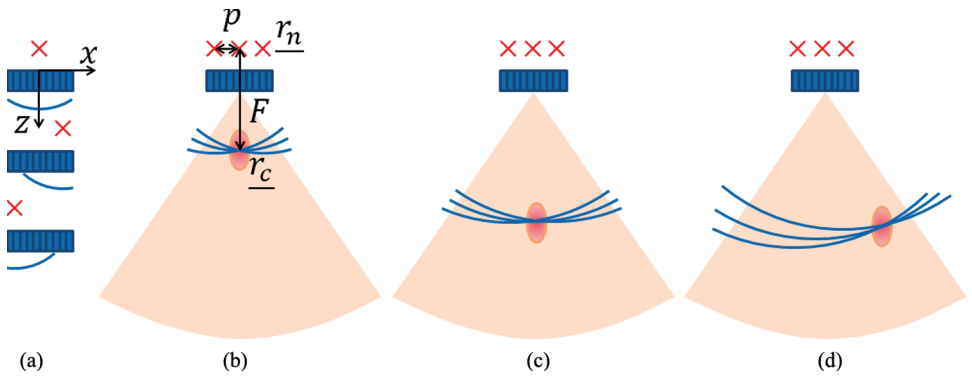

Fig. 1. Principle of coherent compounding with diverging waves. (a) Three diverging waves defined by their virtual source (red crosses at $\underline{r_n}$) spaced by a virtual pitch p, are sent independently with a phased array probe directly in contact with the region of interest. Each diverging wave is backscattered by heterogeneities and the array receives the corresponding echo. Beamforming is performed, applying delays corresponding to a constructive interference of these diverging waves at the focal point $\underline{r_c}$. (b) By changing the delay applied to each of the backscattered echoes from (a), the resulting waves can interfere and virtually focus at different depths, as in (c), and lateral positions, as in (d).

$$X_0 = \frac{\lambda F}{pN} l, \quad l \in \mathbb{Z} - \{Nk'; k' \in \mathbb{Z}\}, \tag{4}$$

where the wavelength λ is given by $(2\pi)/k$. We see in (4) that the width of the principal lobe decreases with the total aperture of the virtual array, which results in an improvement of the lateral resolution as the number of transmits or the virtual pitch increases.

Global maxima of the pressure field occur when

$$\frac{kp}{2F} X = l\pi, \quad l \in \mathbb{Z} \tag{5}$$

$$\Rightarrow X_{\max} = \frac{\lambda F}{p} l, \quad l \in \mathbb{Z}. \tag{6}$$

$X_{\max}$ is the position of grating lobes. Eq. (6) shows that as the pitch p between virtual sources decreases, the grating lobes are rejected farther from the focus ($X_{\max}$ becomes larger).

To be strictly accurate, the element width and the subaperture size should be considered in this derivation. Furthermore, it is only true for compounding on the central line in the far field. Therefore, at a distance of several centimeters, this equation can be used to investigate the focus and the grating lobes at a lateral distance of several millimeters. However, the derivation gives an idea of how the synthetic pressure field varies in terms of maxima and zeros with respect to the number of virtual sources and their position, which shows that the total aperture should be maximized to increase the lateral resolution and the distance between sources should be minimized to decrease the grating lobes.

B. Numerical Simulations

A standard phased-array probe of 64 elements with 0.28-mm pitch, 13-mm height, a center frequency of 2.7-MHz (100% bandwidth), and a 60-mm elevation focus was implemented in Field II [31], [32]. The coordinates of the elements were set as $\begin{pmatrix} x_e \\ 0 \\ 0 \end{pmatrix}$. The sampling frequency of acoustic pulses was 200 MHz. The acoustic field transmitted from each virtual source placed behind the probe was calculated using Field II. For more than one transmit, spatial coherent compounding was performed as shown in Fig. 1. More specifically, the transmit delays associated with the virtual source coordinates $\begin{pmatrix} x_n \\ 0 \\ z_n \end{pmatrix}$ were calculated as

$$\text{delay} = \sqrt{{z_n}^2 + (x_e - x_n)^2}/c, \tag{7}$$

where c is the speed of sound in soft tissues (1540 m·s^{-1}). Simulations of the synthetic acoustic field (the acoustic field from each transmit summed with spatial coherent compounding) were performed to investigate the dependence of the virtual sources upon the position, the size of the transmit apertures (subapertures), and the number of virtual sources.

C. Angular Aperture and Transmit Subapertures

The angular aperture of the transmitted beam is important to define the field of view achieved in the final image. In this study, we assume that the transmitted wave must be symmetrical and homogeneous over the entire sector image. Therefore, the virtual point source must be placed at the center of the transmit subaperture (e.g., Fig. 2). The angular aperture for each transmit is defined geometrically by

$$\theta_{\text{aperture}} = 2 \arctan\left(\frac{a/2}{|z_n|}\right). \tag{8}$$

where a is the size of the subaperture (number of elements which participate in the diverging wave transmission, as

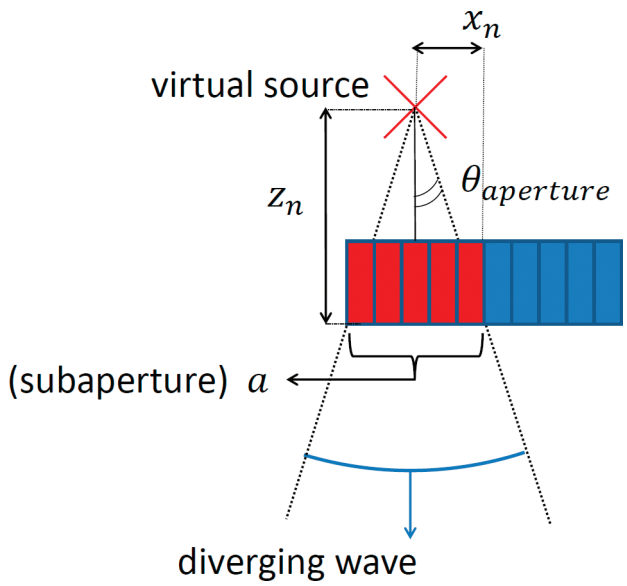

Fig. 2. The virtual source is placed at a distance z_n from the probe. It is placed at the center of the subaperture a. The diverging wave is transmitted over the entire field of view.

shown in Fig. 2) and z_n is the virtual source position on the z-axis relative to the ultrasound probe.

Fig. 3 shows the synthetic pressure field from three diverging waves. Coherent summation was performed at a 60-mm depth at two extreme lateral positions of the field of view: on the central line [Fig. 3(top)] and on the edge of a 90° sector [Fig. 3(bottom)]. Three different transmitted angular apertures are shown (70°, 90°, 110°). The angular aperture variation was obtained by varying z_n, with subapertures of 21 elements. Lateral positions of the virtual sources were placed in the middle of the 21 elements subapertures respectively at a position $x_n = [-5.9;0;5.9]$ mm.

The left-hand side of Fig. 3 shows the synthetic pressure distribution on an arc of circle at a 60 mm depth where coherent summation is made. The right-hand side of Fig. 3 shows this pressure distribution in the entire space.

Approximately the same focus is obtained on the central axis with the three angular apertures, whereas the off-axis focusing capacity varies with the angular aperture. The steering capability depends strongly on the angular transmit aperture. Fig. 3 shows that an angular aperture of more than 90° is required to decrease the grating lobes generated on the central axis and to achieve a good focusing on the off-axis position at $\pi/4$ (which is a large imaging sector configuration).

The other important dimension of the transmit aperture is its physical extent on the transducer array. This parameter has been investigated by Lockwood *et al.* [26], who showed that the signal-to-noise ratio improved with the square root of the number of elements as $\sim N^{1/2}$.

Fig. 4 shows the pressure field 60 mm away from the transducer as a function of the size of the transmit subaperture. The subapertures were defined in numbers of elements. One virtual source was placed at their center. The virtual source position on the z-axis was varied, regarding subaperture size, to keep an angular aperture of 90°. As shown in Fig. 4, the transmitted pressure increases with the number of elements. With only one transmit element, such as in conventional synthetic aperture imaging, less than 10% of the pressure transmitted by the entire array is obtained. On the other hand, large subapertures do not allow a large virtual pitch p (because virtual sources are placed at the center of subapertures), which is required to improve the lateral resolution (4). Therefore, to maximize the resolution, the transmit subaperture must be as small as possible. A transmit subaperture of approximately 20 elements is a good tradeoff to obtain a high pressure

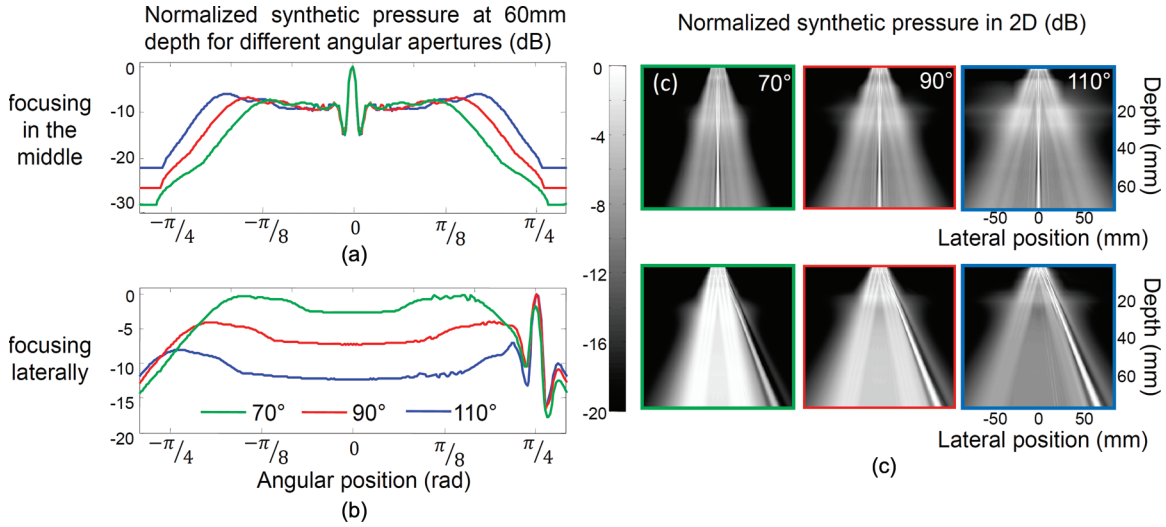

Fig. 3. Normalized synthetic pressure field for three angular apertures (70°, 90°, and 110°). Three virtual sources were placed at ($x_n = [-5.9;0;5.9]$ mm) with subaperture of 21 elements centered on each virtual source. Coherent summation was performed at a depth of 60 mm (a) on the central axis and (b) on the side at 60 mm. (c) 2-D normalized synthetic pressure distribution obtained for the different configurations.

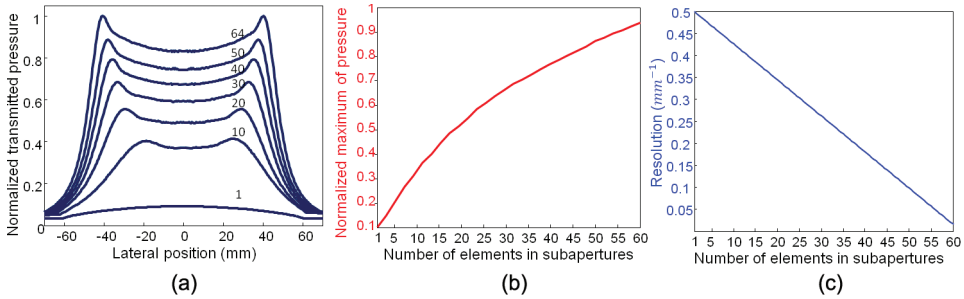

Fig. 4. (a) Simulation of the normalized pressure field of one diverging wave for an angular sector of 90° at a depth of $R = 6$ cm for increasing number of transmit elements (1 to 64). (b) Simulated maximum synthetic pressure and (c) resolution when three sources located at the center of the subaperture were used, as a function of subaperture size (red plot). (c) The associated resolution (inverse of the main lobe −6-dB width) when virtual sources were placed at the center of subaperture is plotted in blue.

(more than half of the pressure transmitted with the entire probe) and a wide variety of possible virtual source positions [Figs. 4(b) and 4(c)].

D. Lateral Positions of the Virtual Sources

Fig. 5 represents the synthetic transmitted pressure field obtained for three different virtual source pitches. Three diverging waves were used and coherent summation was performed at a 60-mm depth at two lateral positions in the field of view: on the central line [Fig. 5(top)] and on the edge of a 90° sector [Fig. 5(bottom)]. The angular aperture (100°) and the subaperture (21 elements) were kept constant. A virtual source was placed on the central axis and the two others are placed symmetrically at a varying distance (1.4, 2.8, and 5.6 mm). In agreement with (4), we found that the lateral resolution increases with the virtual source pitch. The widths of the main lobe at −6 dB are 11, 5.5, and 2.8 mm, respectively. On the other hand, the grating lobes move closer to the focus when the spacing is enlarged. This is in good agreement with the grating lobe position derived from (6).

E. Number of Diverging Waves

Because the number of transmitted waves determines the maximum frame rate achievable, it is important to determine how fast the image quality improves with the number of diverging waves in ultrafast imaging applications. The virtual sources were placed behind the probe at a distance $z_n = 2.94$ mm. Each virtual source was positioned at the center of a 21-element subaperture [e.g., Fig. 2(a)]. These parameters were set to get a 90° angular aperture according to (8). The first virtual source was placed at $x_n = 0$ (center of transducer array). The number of diverging waves was then increased by adding virtual sources around the first virtual source placed at the center. For three transmits, we added two virtual sources on the edge of the transducer array ($x_n = [-5.9; 0; 5.9]$-mm). This way, the distance between the two extreme sources was maximized to get a good resolution and allowed positioning of the sources in the middle of a 21 elements subaperture. Then two virtual sources were added between the previous three to obtain five transmits (lateral source positions $x_n = [-5.9; -2.95; 0; 2.95; 5.9]$ mm) and so on.

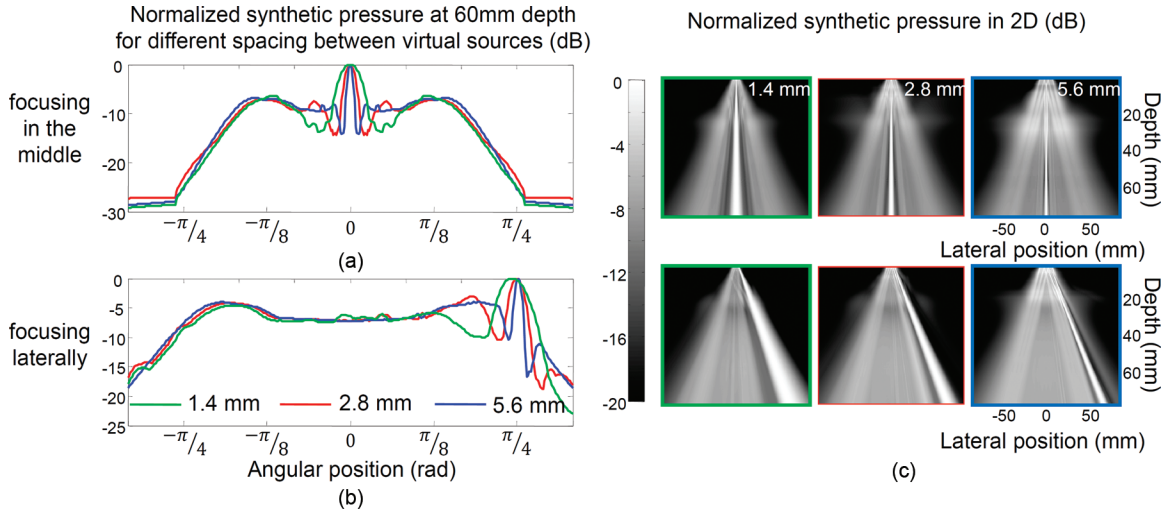

Fig. 5. Normalized transmitted pressure field for different virtual pitch (p). The virtual sources were placed at the center of 21 element subapertures. Three different distances between virtual sources (1.4, 2.8, and 5.6 mm) are compared. Coherent summations made at a depth of 60 mm (a) on the central axis and (b) on the side at 60 mm are compared. (c) 2-D normalized synthetic pressure distribution obtained for the different configuration.

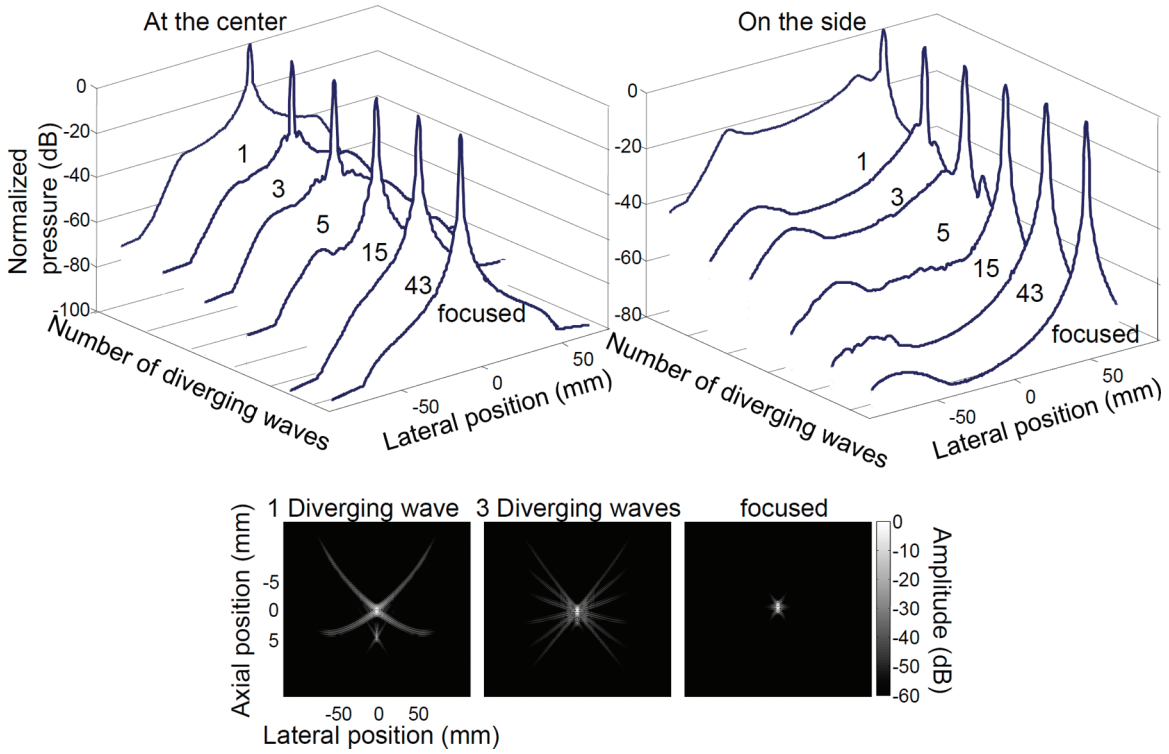

Fig. 6. Normalized synthetic pressure field at two points of space (center, side) for a 90° sector at a 60-mm depth against lateral position. The transmit-receive synthetic fields induced by compounding 1, 3, 5, 15, and 43 diverging waves are presented and compared with the focused emission. Side lobes and mean level decrease when the number of diverging waves increases and converge toward focused emission. Normalized PSFs for 1 and 3 diverging waves and focused waves at the center were also simulated.

Additionally, conventional focusing in reception was performed at the transmit focus location to investigate the final image quality.

Fig. 6 shows the focusing quality improvement with the number of transmits [on pressure amplitude and point spread function (PSF)]. The pressure level at the center axis was evaluated for the steered focus. We found −24 for one diverging wave, and −42.4, −51.2, −60.3, and −68.1 dB for 3, 5, 15, and 43 diverging waves, respectively. A large improvement is achieved with only 3 transmits, particularly off-axis, where the mean pressure level is reduced by 18.4 dB. Focusing is then progressively improved with the number of transmits, and with 43 transmits, the focus becomes comparable to conventional focusing. The normalized PSFs for 1 and 3 diverging waves and focused waves are also displayed to illustrate the improvement. It shows that with coherent compound imaging a small number of transmits enables a major improvement of the focusing quality while maintaining a high frame rate.

III. Experiments

A. Coherent Diverging-Wave Compounding in a Heart Phantom

The imaging quality was assessed experimentally in a heart phantom (model 067, Computerized Imaging Reference Systems Inc., Norfolk, VA). A standard phased array probe (64 elements, 2.7-MHz central frequency, Vermon S.A., Tours, France) with the same characteristics as the one used in simulations was used to image the phantom. The technique of coherent diverging-wave compounding was implemented in real time on an ultrafast scanner (Aixplorer, SuperSonic Imagine, Aix-en-Provence, France). The imaging depth was set to 12 cm. The number of emitted diverging waves was varied from 1 to 20 diverging waves, providing a frame rate between 4600 and 230 frames/s, respectively. A sequence with conventional focusing in transmit (160 focused transmits at 60 mm) was also used for comparison. In reception, conventional, dynamic-focusing beamforming with full aperture was performed for all acquisitions. The magnitude of the beamformed IQ data was normalized. Each depth was normalized by the maximum magnitude at that depth. It was then scan-converted and log-compressed to obtain the final B-mode image with a 50-dB dynamic range. This normalization provides the contrast variation as a function of depth.

The angular aperture was set to 90°, the subapertures were composed of 21 elements, and virtual source positions (x_n) were the same as in Section II-E.

Fig. 7 shows the improvement of the imaging quality with the number of diverging-wave transmits. One can observe the improvement of both the lateral resolution and the SNR between the image made by transmitting a single diverging wave [Fig. 7(a)] and images made of several transmits [Fig. 7(b)–7(d)]. A strong improvement is found

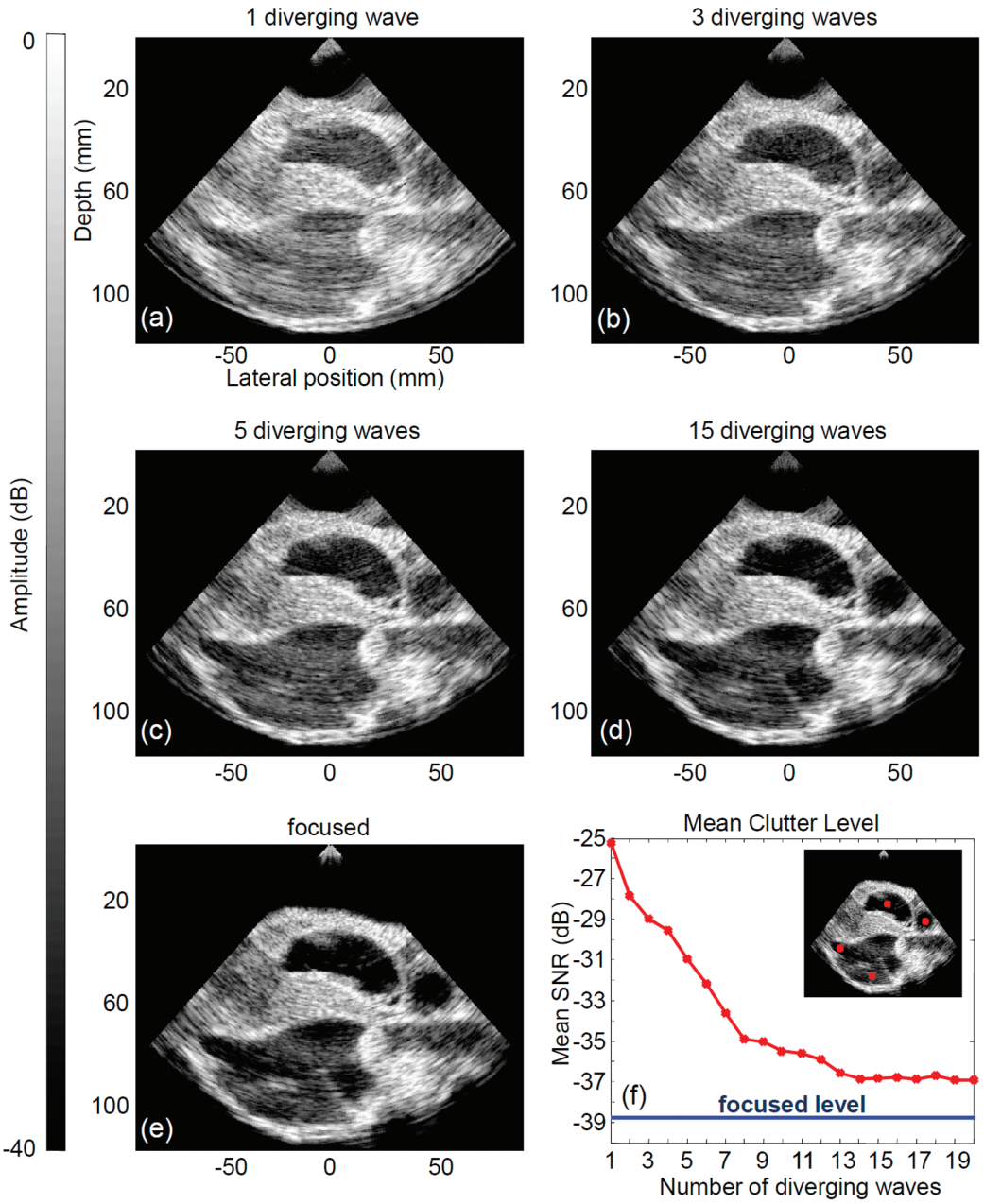

Fig. 7. Comparison between four configurations using (a)–(d) different numbers of diverging waves and (e) conventional focusing on a heart phantom. (f) The average clutter signal level was evaluated at several positions shown by the boxes.

for configurations relying on a small number of transmits, e.g., 3 or 5. With only 15 diverging waves [e.g., Fig. 7(d)] the image quality is qualitatively comparable with the one obtained with conventional focusing [e.g., Fig. 7(e)]. The mean clutter level was assessed by averaging the absolute magnitudes of normalized images in the four cardiac cavities [red squares in Fig. 7(f)]. Fig. 7(f) shows a large improvement in the SNR (−25 dB to −36.5 dB) when the number of waves is first increased from 1 to 15 diverging waves, after which the improvement becomes less important (−36.5 dB to −37 dB from 15 diverging waves to 20 diverging waves). The clutter level of conventional focusing was also assessed (38.5 dB). With only 15 diverging waves, the SNR is only 2 dB lower than the SNR of the focused mode. Nevertheless, the important result here is the improvement of clutter level in the ultrafast imaging range, i.e., 1 to 10 diverging waves. For example, to achieve very high frame rates (~1000 images/sec) at a 12 cm depth, the number of transmits cannot exceed 5.

B. Ultrafast Imaging of Shear Wave Propagation

Coherent compounding of diverging waves was evaluated for imaging the propagation of shear waves at very high frame rate. Two different sequences were designed. The first sequence shows the improvement of coherent compounding; the second shows the impact of the angular aperture.

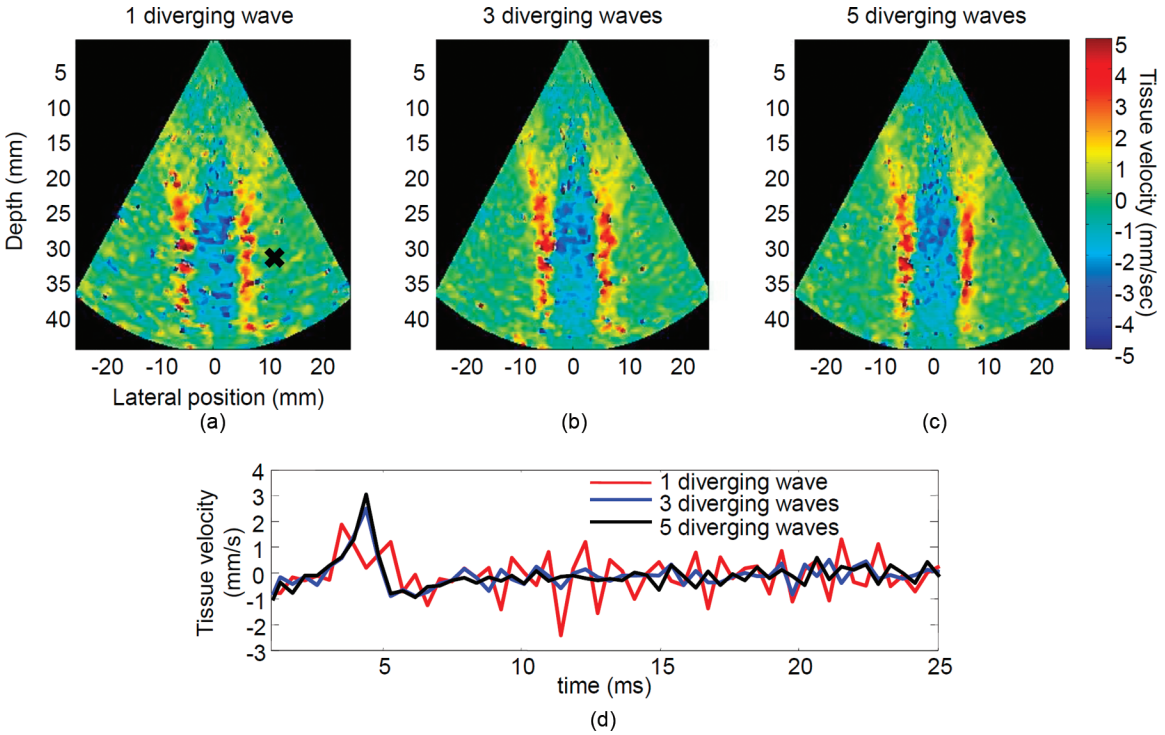

Fig. 8. Tissue velocity images of shear wave propagation at 1.6 ms after the push. Imaging with (a) one, (b) three, and (c) five diverging wave(s) with the spatial coherent compound method. (d) The tissue velocity at one point of space (black cross) is plotted against time for the three configurations.

1) Number of Transmits: The phased array probe described in Section III-A was used to image a breast phantom (CIRS, model 059), in which the shear wave velocity is approximately 2.3 m/s, and two phantoms made of agar-gelatin (2%–2% and 2%–10%), in which shear waves propagate at 1.3 m/s and 5.5 m/s, respectively. A sequence was designed to remotely generate shear waves based on the radiation force induced by a focused ultrasonic burst [33], [34]. The pushing depth and duration were set at 30 mm and 300 μs, respectively. To image the shear wave propagation, 100 frames were acquired at the frame rate of 2500 frames/s. The experiment was repeated three times in each phantom. The imaging depth was set to 45 mm and the pulse repetition frequency (PRF) was the same for all the acquisitions (12 500 Hz). Different transmit schemes were used to compare the performances of 1, 3, and 5 virtual sources while keeping the same total number of transmits to highlight the influence of focalization resulting from the spatial coherent compounding. For one virtual source, transmission was repeated at the same PRF and five successive acquisitions were averaged to form one image. With three virtual sources positioned laterally at $[-5.9; 0; 5.9]$ mm, the three different transmits were performed successively followed by two additional lateral transmits, and the five acquisitions were used to form one compound image. Finally, five virtual sources located at $[-6.7; -3.35; 0; 3.35; 6.7]$ mm laterally and at a distance of 3 mm behind the probe were transmitted and used to form one image. Because shear waves propagate over a relatively small distance, the imaging sector size was reduced and the angular aperture associated with each virtual source was set to 70°. Tissue velocities were obtained using a per-pixel frame-to-frame 1-D cross-correlation on demodulated IQ images with an axial kernel size of 3 pixels (1.5 mm) to obtain images of frame-to-frame axial tissue displacements. Fig. 8 shows the tissue velocity generated by the shear wave during its propagation. An increase in the SNR of the tissue velocity estimation and of the lateral resolution with the number of virtual sources can be observed.

The SNR improvement can be seen in Fig. 8(d). Fluctuations are more important when only one diverging wave is used.

To quantify the improvement of tissue velocity estimations in the entire image, the SNR was calculated as follows for each set of acquisition and for the three different phantoms:

$$\overline{\mathrm{SNR}} = \frac{\langle S_0(x,z)\rangle}{\sigma_{xz}} \tag{9}$$

$$S_0(x,z) = \max_{(t)}(S(x,z,t)). \tag{10}$$

TABLE I. MEAN SNRS FOR DIFFERING NUMBERS OF DIVERGING WAVES.

Gel speed (m/s)	1 wave (dB)	3 waves (dB)	5 waves (dB)
1.3	26.4	28.1	30
2.3	16.1	17.1	19.1
5.5	16.5	17.6	18.5

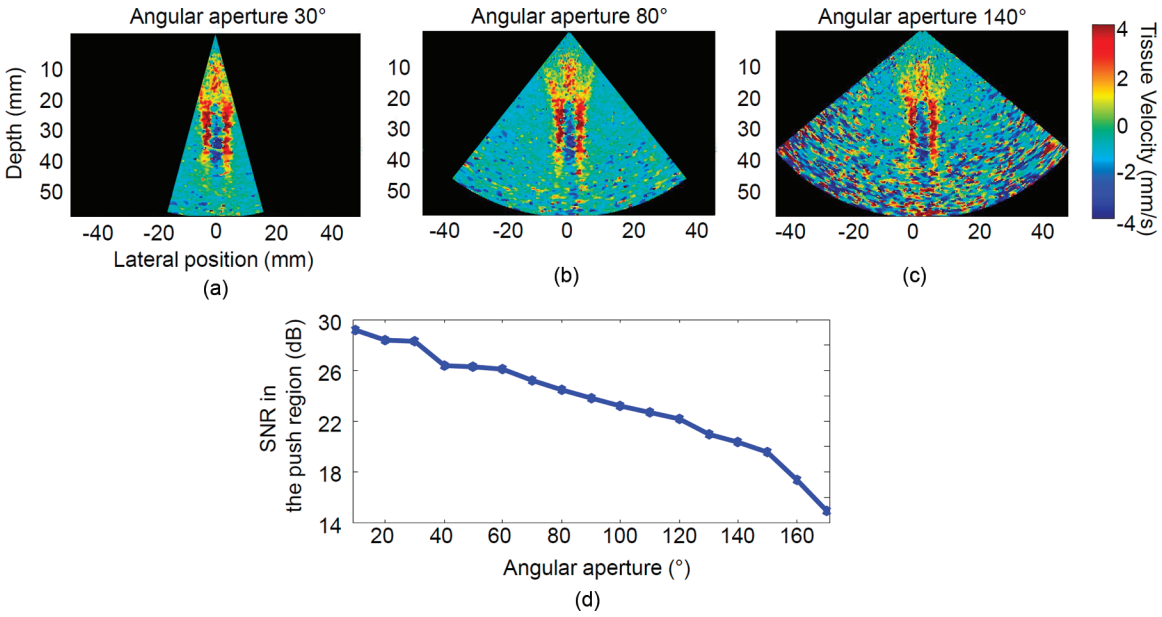

Fig. 9. Three acquisitions with angular apertures of (a) 30°, (b) 80°, and (c) 140° are imaged. The SNR within the push region is quantified for angular apertures from 10° to 140°.

S is the tissue velocity of the shear wave and the amplitude of fluctuations is given by

$$\sigma_{xz} = \sqrt{\sum_{t+\mathrm{d}t} (S(x,z,t) - S(x,z,t))^2}, \tag{11}$$

where $t + \mathrm{d}t$ is the time after the shear wave propagation. The mean SNR is presented in Table I and shows a significant improvement of the SNR with the number of individual virtual sources. This increase is less important in stiffer gels because of the higher shear wave speed, lower

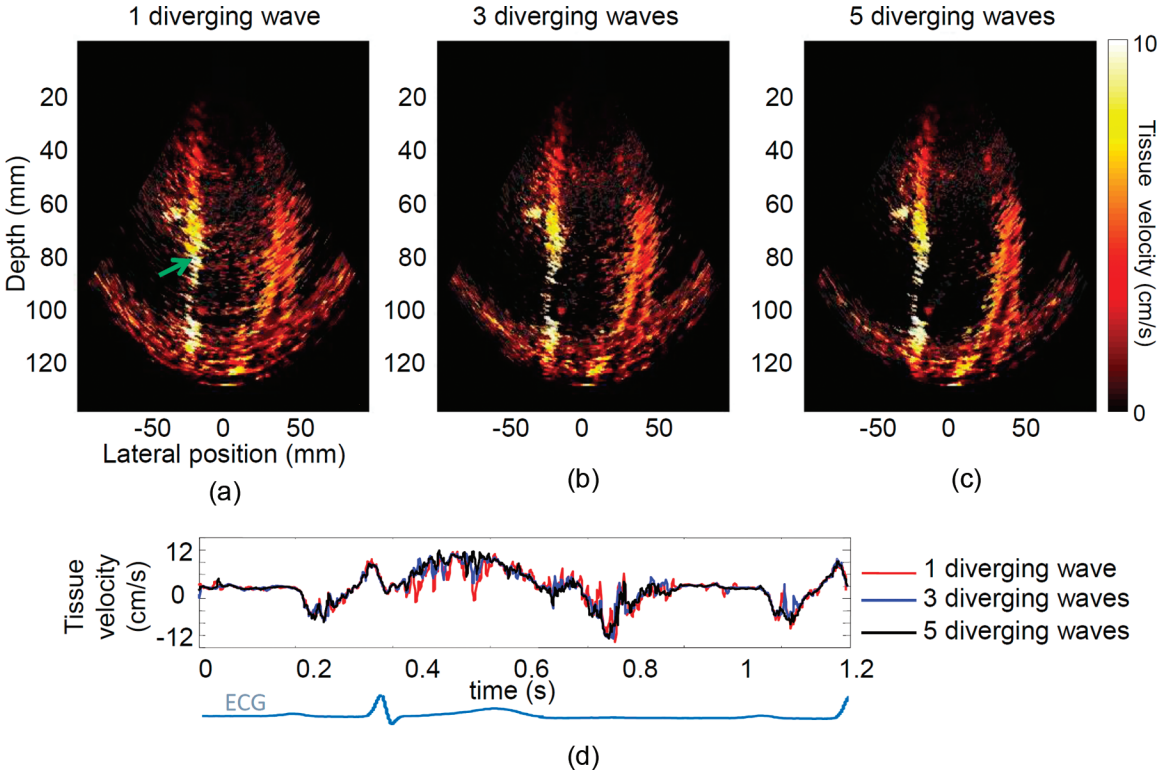

Fig. 10. Tissue velocity map in an *in vivo* normal human heart superimposed on the B-mode image, both obtained using (a) 1, (b) 3, and (c) 5 diverging waves. (d) The tissue velocity at one point of space (green arrow) is plotted against time for the three configurations. The cineloop shows the tissue velocity in an *in vivo* human heart superimposed on the B-mode image for three configurations (1, 3, and 5 diverging waves) for one cardiac cycle.

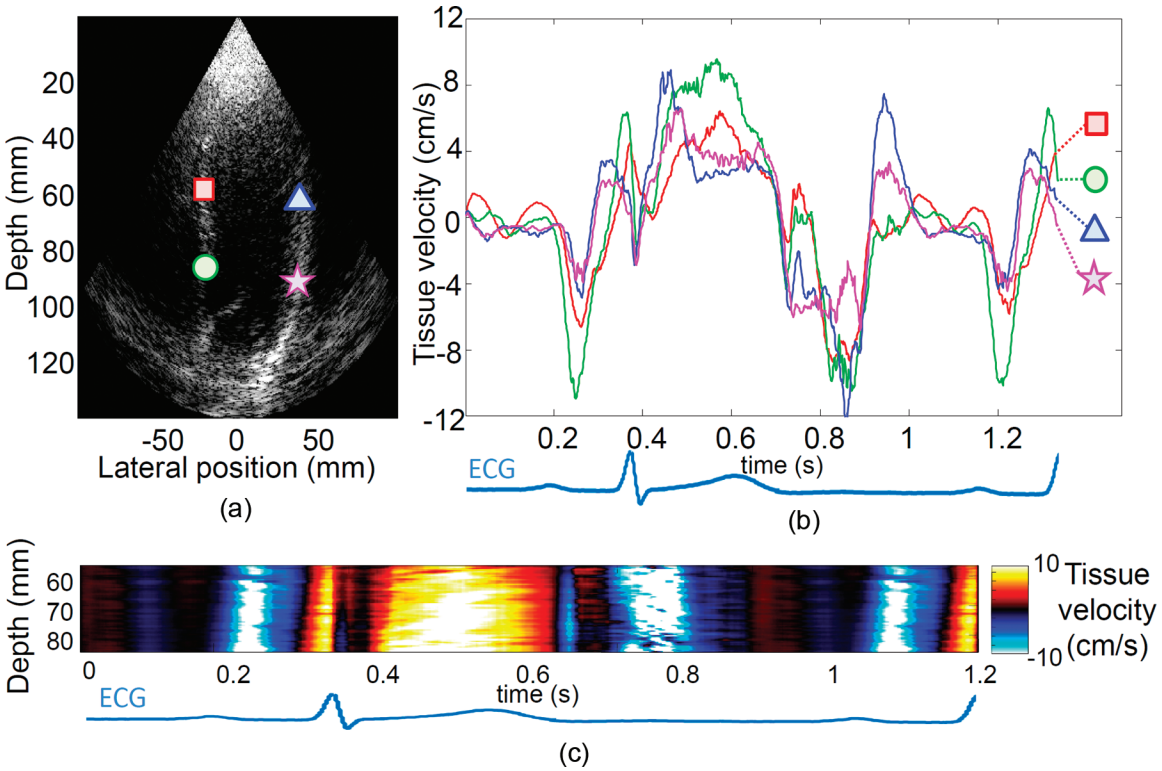

Fig. 11. (a) Four different locations in the the heart and (b) their associated tissue velocities. (c) Spatial and temporal tissue velocities along the septum over one cardiac cycle.

tissue velocities, and the competition between frame rate and tissue velocity estimation.

2) Angular Aperture and SNR: The dependence of the SNR on the transmitted angular aperture was investigated. With the same phased-array probe, shear-wave imaging acquisition was performed with a pushing depth and duration set to 30 mm, and 300 μs, respectively. To image the shear wave propagation, 100 frames were acquired at the frame rate of 2000 frames/s. The experiment was repeated three times. The imaging depth was 55 mm and the PRF was kept the same for all the acquisitions (10 000 Hz). Laterally, five virtual sources were positioned at the location described in Section-III-B-1. Different transmit schemes were used to compare the performances of angular apertures varying from 10° to 170°. Figs. 9(a)–9(c) show a large difference in terms of SNR between the different angular apertures. Fig. 9(d) quantifies the SNR in the push region as a function of angular aperture. Higher SNR is obtained by reducing the angular aperture.

C. In Vivo Ultrafast Imaging in a Large-Sector View of the Human Heart

Finally, we investigated the performance of ultrafast imaging of the human heart *in vivo*. The transthoracic phased array probe described in Section III-A is placed to visualize the entire left ventricle in an apical two-chamber view. A standard focused B-mode running in real time at 30 frames/s was used to position the probe. An ultrafast sequence was performed on the Aixplorer with 5 diverging waves with the virtual source positions described in Section III-A. The PRF was set to 4500 Hz, resulting in a frame rate of 900 frames/s. The acquisition was triggered on the ECG. We recombined the backscattered signals off-line using three different approaches. The first set of images was obtained by using only the central transmit acquisition (one virtual source laterally placed in the middle of the probe). Then, the second set was obtained by spatial coherent compounding of three virtual sources. Finally, the third set was obtained by applying the spatial coherent compounding method on five diverging waves.

For each set, a standard frame-to-frame correlation technique was used to derive the tissue velocities in the myocardium over time [33]. Fig. 10 shows the velocity field combined linearly to the B-mode; a cine-loop ( ) is attached to the figure. An improvement of the image quality was observed as the number of compounded waves was increased, both in terms of contrast and resolution, along with a reduction of the clutter signal level. The tissue velocity noise level also decreased as the number of waves was increased (*d*). This shows the possibility of improving the image quality over a large field of view while maintaining a high frame rate over one cardiac cycle, which is important for imaging applications such as electromechanical and mechanical wave imaging (e.g., Fig. 11).

Fig. 11 demonstrates the feasibility of obtaining good tissue velocity estimation at every location of the heart in the same acquisition.

IV. Discussion

In this paper, ultrafast imaging was performed using diverging waves transmitted by a conventional phased-array probe over a large imaging sector. The method proposed here allows improvement of the contrast and resolution for an ultrafast acquisition at very high frame rate (more than 1000 images/s). It should be noted that the imaging quality remains less than that which can be achieved with high-contrast echocardiography at conventional frame rates. However, the image quality was found to improve rapidly with the number of transmits, which allows maintenance of a high frame rate, a large imaging sector, and a large SNR simultaneously.

The focusing quality was investigated as a function of the virtual source positions and the technique was implemented on a commercial scanner.

The feasibility of improving the imaging quality at a high enough frame rate to image the propagation of shear waves in the myocardium was shown in this study. Shear waves remotely induced by the phased-array probe were imaged in a phantom at a depth of 45 mm at 2500 frames/s using 5 diverging waves. At such an imaging depth, the anterior wall of the left ventricle, for example, should be reached in most patients in a parasternal long-axis view to generate shear waves propagating along the septum or anterior wall. For imaging at larger depth, the number of compounded waves must be reduced to two or three to maintain the frame rate. Because the quality of tissue velocity estimation is crucial to correctly image the shear wave propagation, these results are promising and should help for the noninvasive real time elasticity mapping of the human anterior wall.

We have also shown that spatial coherent compounding may allow imaging of the propagation of mechanical waves in tissues resulting from the valves' closures and electromechanical waves (typical speed in the range of 1 to 5 m/s) with higher quality. The electromechanical activation has been imaged at typical frame rates of 800 to 2000 images/s using single diverging waves [36], [37]. Using 5 waves, we have shown *in vivo* in the human heart a strong improvement of both the B-mode and the velocity estimation quality compared with one diverging wave imaging.

One important issue to deal with is the influence of motion artifacts on the coherent summation of backscattered echoes from successive virtual sources, as pointed out by different groups [38]–[40]. Because fast tissue motion can occur during the cardiac cycle, the degradation of coherent summation should be taken into account. Although a small number of diverging waves should not be influenced by motion because the acquisition of the successive set of backscattered echoes is performed before significant tissue motion, this problem could become critical for a large number of transmit diverging waves. One way to estimate the maximum number of compounded diverging waves that can be used without affecting the image quality of the compounded image is to consider the intensity loss at the synthetic focus obtained by coherent summation of images caused by motion artifacts between the first and last compounded diverging wave transmission. It is known from the diffraction theory [41] that the loss of wave intensity at the focus is equal to $1 - \sqrt{1 - ((2\pi)/\lambda)^2(\delta/4)^2}$ where δ is the aberration amplitude. For example, if we arbitrarily set the maximal intensity loss to 15%, aberration amplitudes must be smaller than $\delta = \lambda/6$ (from $-\lambda/12$ to $\lambda/12$). In that case, it becomes possible to estimate the maximum number of compounded diverging waves that can be used for a desired imaging depth and a maximum velocity while satisfying this criterion (one should note that such a criterion on the compounded image quality is much more severe than a criterion on the quality of the tissue velocity estimate). Fig. 12 presents the number of diverging waves that can be used with respect to imaging depth (and consequently PRF) and maximum velocity estimation. Note that an $N = 5$ number of diverging waves permits an estimation of 15 cm/s maximum tissue velocities for a 10 cm imaging depth while preserving any significant effect on the compounded ultrasonic image quality and consequently tissue velocity estimation.

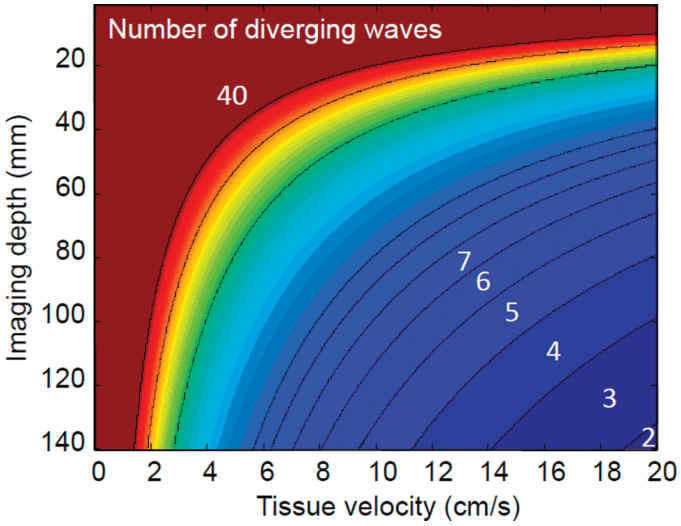

Fig. 12. Maximum number of diverging waves insuring a motion artifact smaller than $\delta = \lambda/6$ between the first and last plane wave transmission as a function of imaging depth and local tissue velocity, for a frequency of 2.5 MHz. The normal and physiological ranges for longitudinal myocardial velocities are in the range 2 to 15 cm/s.

Doppler imaging of cardiac blood flows could also greatly benefit from this technique. Blood flow mapping in the heart is a very demanding application that requires a large field of view, a high frame rate, and an excellent imaging quality to lower the clutter signal originating from the heart walls. Coherent compounding with diverging waves at high frame rate could be used to map the flow pattern in the ventricles and obtain Doppler spectrum for each point of the map. Another advantage of such a compounded high-frame-rate acquisition would be to provide both tissue and blood velocities simultaneously [42]. This

particular implementation of the technique will be presented in a future work.

Finally, the concept of compounded diverging waves could be also extended to other types of arrays. For example, plane wave coherent compounding with linear arrays has the disadvantage of reducing the field of view on the sides of the images because the different plane wave transmits don't overlap. Diverging waves with small angular apertures would enable to regain the entire field of view of the image.

V. Conclusion

We have investigated the use of spatial coherent compounding with diverging waves to obtain very-high-frame-rate acquisition of the heart while maintaining high tissue velocity estimation quality over a large field of view. Simulations revealed that by optimizing the location of virtual sources, the image quality can be improved strongly with a few transmits. The technique has been implemented on an ultrasound scanner for cardiac applications and experiments were performed in phantoms with a cardiac phased array probe to quantify and validate the improvement predicted by simulations. Motion and elasticity maps obtained using spatial coherent compounding with diverging waves in phantoms during shear wave imaging resulted in higher SNR and resolution than with single-source acquisitions. Finally, the method was used in the human heart noninvasively over a large field of view during entire cardiac cycles at ultrafast frame rate (900 frames/s). Improvements in image quality were consistent with simulations and phantom studies. This technique has a strong potential to significantly improve the imaging of natural waves such as electromechanical waves and remotely-induced shear waves for elasticity mapping in the human heart in real time.

Appendix

The expression of the acoustic field $\Phi(\underline{\boldsymbol{r}})$ when coherent summation of the acoustic fields generated by each diverging wave at a point $\underline{r_c}\begin{pmatrix} x_c \\ 0 \\ z_c \end{pmatrix}$ of space over the bandwidth (k_1, k_2) is made is as follows:

$$\Phi(\underline{r}) = \int_{k_1}^{k_2} A(k) \sum_{n=-m}^{m} \frac{e^{jk|\underline{r}-\underline{r_n}|}}{|\underline{r}-\underline{r_n}|} \cdot e^{-jk|\underline{r_c}-\underline{r_n}|} \mathrm{d}k. \quad \text{(A1)}$$

In the far-field approximation, at a certain distance of the probe, near the central line $x = 0$, we can assume that $|z_c - z_n| \gg |x - x_n|$. Let's consider the central line at a distance $z_c - z_n = F$.

Approximation can be made on the amplitude:

$$\begin{aligned} |\underline{r}-\underline{r_n}| &= ((x-x_n)^2 + (z-z_n)^2)^{1/2} \\ &= (z-z_n)\left(1 + \frac{(x-x_n)^2}{(z-z_n)^2}\right)^{1/2} \approx (z-z_n) = F. \end{aligned}$$

Approximation can also be made on the phase:

$$\begin{aligned} |\underline{r}-\underline{r_n}| &= ((x-x_n)^2 + (z-z_n)^2)^{1/2} \\ &= (z-z_n)\left(1 + \frac{(x-x_n)^2}{(z-z_n)^2}\right)^{1/2} \\ &\approx (z-z_n) + \frac{1}{2}\frac{(x-x_n)^2}{(z-z_n)} \\ &= F + \frac{1}{2}\frac{(x-x_n)^2}{F}. \end{aligned}$$

Therefore,

$$\Phi(x) \approx \int_{k_1}^{k_2} A(k) \frac{1}{F} \sum_{-m}^{m} e^{jk(F+(x-x_n)^2/2F)} e^{-jk(F+(x_c-x_n)^2/2F)} \mathrm{d}k. \quad \text{(A2)}$$

We can develop the expression

$$\Phi(x) \approx \int_{k_1}^{k_2} A(k) \frac{1}{F} \sum_{-m}^{m} e^{jk(F+(x^2+x_n^2-2xx_n)/2F)} e^{-jk(F+(x_c^2+x_n^2-2x_cx_n)/2F)} \mathrm{d}k. \quad \text{(A3)}$$

Rearranging this expression, we obtain

$$\Phi(x) \approx \int_{k_1}^{k_2} A(k) \frac{1}{F} e^{j(k/(2F))(x^2-x_c^2)} \sum_{-m}^{m} e^{j(k/F)x_n(x_c-x)} \mathrm{d}k. \quad \text{(A4)}$$

For our periodic virtual sources array $x_n = np$:

$$\Phi(x) \approx \int_{k_1}^{k_2} A(k) \frac{1}{F} e^{j(k/(2F))(x^2-x_c^2)} \sum_{-m}^{m} e^{j(k/F)np\ (x_c-x)} \mathrm{d}k. \quad \text{(A5)}$$

$\sum_{-n}^{n} e^{j(k/F)np\ (x_c-x)}$ is a geometrical series that can be added explicitly, and we end up with

$$\Phi(x) \approx \int_{k_1}^{k_2} A(k) \frac{1}{F} e^{j(k/(2F))(x^2-x_c^2)} \frac{\sin(kp(x-x_c)(2m+1)/2F)}{\sin(kp(x-x_c)/2F)} \mathrm{d}k. \quad \text{(A6)}$$

Finally, this leads to (2).

References

[1] J. D'hooge, A. Heimdal, F. Jamal, T. Kukulski, B. Bijnens, F. Rademakers, L. Hatle, P. Suetens, and G. R. Sutherland, "Regional strain

and strain rate measurements by cardiac ultrasound: Principles, implementation and limitations," *Eur. J. Echocardiogr.*, vol. 1, no. 3, pp. 154–170, Jan. 2000.

[2] G. R. Sutherland, B. Bijnens, and W. N. McDicken, "Tissue Doppler echocardiography: Historical perspective and technological considerations," *Echocardiography*, vol. 16, no. 5, pp. 445–453, Jul. 1999.

[3] M. Couade, M. Pernot, E. Messas, A. Bel, M. Ba, A. Hagege, M. Fink, and M. Tanter, "In vivo quantitative mapping of myocardial stiffening and transmural anisotropy during the cardiac cycle," *IEEE Trans. Med. Imaging*, vol. 30, no. 2, pp. 295–305, Feb. 2011.

[4] R. R. Bouchard, S. J. Hsu, M. L. Palmeri, N. C. Rouze, K. R. Nightingale, and G. E. Trahey, "Acoustic radiation force-driven assessment of myocardial elasticity using the displacement ratio rate (DRR) method," *Ultrasound Med. Biol.*, vol. 37, no. 7, pp. 1087–1100, Jul. 2011.

[5] M. Pernot, M. Couade, P. Mateo, B. Crozatier, R. Fischmeister, and M. Tanter, "Real-time assessment of myocardial contractility using shear wave imaging," *J. Am. Coll. Cardiol.*, vol. 58, no. 1, pp. 65–72, Jun. 2011.

[6] H. Kanai, "Propagation of spontaneously actuated pulsive vibration in human heart wall and in vivo viscoelasticity estimation," *IEEE Trans. Ultrason. Ferroelectr. Freq. Control*, vol. 52, no. 11, pp. 1931–1942, Nov. 2005.

[7] M. Pernot, K. Fujikura, S. D. Fung-Kee-Fung, and E. E. Konofagou, "ECG-gated, mechanical and electromechanical wave imaging of cardiovascular tissues in vivo," *Ultrasound Med. Biol.*, vol. 33, no. 7, pp. 1075–1085, Jul. 2007.

[8] J. Provost, W.-N. Lee, K. Fujikura, and E. E. Konofagou, "Electromechanical wave imaging of normal and ischemic hearts in vivo," *IEEE Trans. Med. Imaging*, vol. 29, no. 3, pp. 625–635, Mar. 2010.

[9] C. Bruneel, R. Torguet, K. M. Rouvaen, E. Bridoux, and B. Nongaillard, "Ultrafast echotomographic system using optical processing of ultrasonic signals," *Appl. Phys. Lett.*, vol. 30, no. 8, pp. 371–373, Apr. 1977.

[10] D. P. Shattuck, M. D. Weinshenker, S. W. Smith, and O. T. von Ramm, "Explososcan: A parallel processing technique for high speed ultrasound imaging with linear phased arrays," *J. Acoust. Soc. Am.*, vol. 75, no. 4, pp. 1273–1282, Apr. 1984.

[11] J.-Y. Lu and J. F. Greenleaf, "Pulse-echo imaging using a nondiffracting beam transducer," *Ultrasound Med. Biol.*, vol. 17, no. 3, pp. 265–281, Jan. 1991.

[12] L. Sandrin, S. Catheline, M. Tanter, X. Hennequin, and M. Fink, "Time-resolved pulsed elastography with ultrafast ultrasonic imaging," *Ultrason. Imaging*, vol. 21, no. 4, pp. 259–272, Oct. 1999.

[13] J.-Y. Lu, J. Cheng, and J. Wang, "High frame rate imaging system for limited diffraction array beam imaging with square-wave aperture weightings," *IEEE Trans. Ultrason. Ferroelectr. Freq. Control*, vol. 53, no. 10, pp. 1796–1812, Oct. 2006.

[14] J. Provost, V. T.-H. Nguyen, D. Legrand, S. Okrasinski, A. Costet, A. Gambhir, H. Garan, and E. E. Konofagou, "Electromechanical wave imaging for arrhythmias," *Phys. Med. Biol.*, vol. 56, no. 22, pp. L1–L11, Nov. 2011.

[15] L. Tong, H. Gao, H. F. Choi, and J. D'hooge, "Comparison of conventional parallel beamforming with plane wave and diverging wave imaging for cardiac applications: A simulation study," *IEEE Trans. Ultrason. Ferroelectr. Freq. Control*, vol. 59, no. 8, pp. 1654–1663, Aug. 2012.

[16] I. K. Ekroll, A. Swillens, P. Segers, T. Dahl, H. Torp, and L. Lovstakken, "Simultaneous quantification of flow and tissue velocities based on multi-angle plane wave imaging," *IEEE Trans. Ultrason. Ferroelectr. Freq. Control*, vol. 60, no. 4, pp. 727–738, Apr. 2013.

[17] M. Tanter, J. Bercoff, A. Athanasiou, T. Deffieux, J.-L. Gennisson, G. Montaldo, M. Muller, A. Tardivon, and M. Fink, "Quantitative assessment of breast lesion viscoelasticity: Initial clinical results using supersonic shear imaging," *Ultrasound Med. Biol.*, vol. 34, no. 9, pp. 1373–1386, Sep. 2008.

[18] M. Muller, J.-L. Gennisson, T. Deffieux, M. Tanter, and M. Fink, "Quantitative viscoelasticity mapping of human liver using supersonic shear imaging: Preliminary in vivo feasibility study," *Ultrasound Med. Biol.*, vol. 35, no. 2, pp. 219–229, Feb. 2009.

[19] M. Couade, M. Pernot, C. Prada, E. Messas, J. Emmerich, P. Bruneval, A. Criton, M. Fink, and M. Tanter, "Quantitative assessment of arterial wall biomechanical properties using shear wave imaging," *Ultrasound Med. Biol.*, vol. 36, no. 10, pp. 1662–1676, Oct. 2010.

[20] T.-M. Nguyen, J.-F. Aubry, D. Touboul, M. Fink, J.-L. Gennisson, J. Bercoff, and M. Tanter, "Monitoring of cornea elastic properties changes during UV-A/riboflavin-induced corneal collagen crosslinking using supersonic shear wave imaging: A pilot study," *Invest. Ophthalmol. Vis. Sci.*, vol. 53, no. 9, pp. 5948–5954, Aug. 2012.

[21] R. R. Bouchard, S. J. Hsu, P. D. Wolf, and G. E. Trahey, "In vivo cardiac, acoustic-radiation-force-driven, shear wave velocimetry," *Ultrason. Imaging*, vol. 31, no. 3, pp. 201–213, Jul. 2009.

[22] M. Tanter, J. Bercoff, L. Sandrin, and M. Fink, "Ultrafast compound imaging for 2-D motion vector estimation: Application to transient elastography," *IEEE Trans. Ultrason. Ferroelectr. Freq. Control*, vol. 49, no. 10, pp. 1363–1374, Oct. 2002.

[23] G. Montaldo, M. Tanter, J. Bercoff, N. Benech, and M. Fink, "Coherent plane-wave compounding for very high frame rate ultrasonography and transient elastography," *IEEE Trans. Ultrason. Ferroelectr. Freq. Control*, vol. 56, no. 3, pp. 489–506, Mar. 2009.

[24] J. A. Jensen, S. I. Nikolov, K. L. Gammelmark, and M. H. Pedersen, "Synthetic aperture ultrasound imaging," *Ultrasonics*, vol. 44, pp. e5–e15, 2006.

[25] C. R. Cooley and B. S. Robinson, "Synthetic focus imaging using partial datasets," in *Proc. IEEE Ultrasonics Symp.*, 1994, vol. 3, pp. 1539–1542.

[26] G. R. Lockwood, J. R. Talman, and S. S. Brunke, "Real-time 3-D ultrasound imaging using sparse synthetic aperture beamforming," *IEEE Trans. Ultrason. Ferroelectr. Freq. Control*, vol. 45, no. 4, pp. 980–988, 1998.

[27] C. R. Hazard and G. R. Lockwood, "Theoretical assessment of a synthetic aperture beamformer for real-time 3-D imaging," *IEEE Trans. Ultrason. Ferroelectr. Freq. Control*, vol. 46, no. 4, pp. 972–980, 1999.

[28] S. I. Nikolov, J. Kortbek, and J. A. Jensen, "Practical applications of synthetic aperture imaging," in *Proc. IEEE Int. Ultrasonics Symp.*, 2010, pp. 350–358.

[29] S. I. Nikolov, "Synthetic aperture tissue and flow ultrasound imaging," Ph.D. dissertation, Orsted-DTU, Technical University of Denmark, Lyngby, Denmark, 2001.

[30] H. Hasegawa and H. Kanai, "High-frame-rate echocardiography using diverging transmit beams and parallel receive beamforming," *J. Med. Ultrason.*, vol. 38, no. 3, pp. 129–140, 2011.

[31] J. A. Jensen, "Field: A program for simulating ultrasound systems," *Med. Biol. Eng. Comput.*, vol. 34, suppl. 1, pt. 1, pp. 351–353, 1996.

[32] J. A. Jensen and N. B. Svendsen, "Calculation of pressure fields from arbitrarily shaped, apodized, and excited ultrasound transducers," *IEEE Trans. Ultrason. Ferroelectr. Freq. Control*, vol. 39, no. 2, pp. 262–267, 1992.

[33] J. Bercoff, M. Tanter, and M. Fink, "Supersonic shear imaging: A new technique for soft tissue elasticity mapping," *IEEE Trans. Ultrason. Ferroelectr. Freq. Control*, vol. 51, no. 4, pp. 396–409, Apr. 2004.

[34] C. Papadacci, M. Pernot, M. Couade, M. Fink, and M. Tanter, "Shear wave imaging of the heart using a cardiac phased array with coherent spatial compound," in *Proc. IEEE Ultrasonics Symp.*, 2012, pp. 2023–2026.

[35] O. Bonnefous and P. Pesqué, "Time domain formulation of pulse-Doppler ultrasound and blood velocity estimation by cross correlation," *Ultrason. Imaging*, vol. 8, no. 2, pp. 73–85, Apr. 1986.

[36] J. Provost, S. Thiébaut, J. Luo, and E. E. Konofagou, "Single-heartbeat electromechanical wave imaging with optimal strain estimation using temporally unequispaced acquisition sequences," *Phys. Med. Biol.*, vol. 57, no. 4, pp. 1095–1112, Feb. 2012.

[37] J. Provost, A. Gambhir, J. Vest, H. Garan, and E. E. Konofagou, "A clinical feasibility study of atrial and ventricular electromechanical wave imaging," *Heart Rhythm*, vol. 10, no. 6, pp. 856–862, Jun. 2013.

[38] K. S. Kim, J. S. Hwang, J. S. Jeong, and T. K. Song, "An efficient motion estimation and compensation method for ultrasound synthetic aperture imaging," *Ultrason. Imaging*, vol. 24, no. 2, pp. 81–99, Apr. 2002.

[39] J. Wang and J. Lu, "Motion artifacts of extended high frame rate imaging," *IEEE Trans. Ultrason. Ferroelectr. Freq. Control*, vol. 54, no. 7, pp. 1303–1315, Jul. 2007.

[40] N. Oddershede and J. A. Jensen, "Effects influencing focusing in synthetic aperture vector flow imaging," *IEEE Trans. Ultrason. Ferroelectr. Freq. Control*, vol. 54, no. 9, pp. 1811–1825, Sep. 2007.

[41] J. W. Goodman, Ed., *Introduction to Fourier Optics*, 2nd ed., New York, NY: McGraw-Hill International Editions, 1996.

[42] J. Luo and E. E. Konofagou, "Imaging of wall motion coupled with blood flow velocity in the heart and vessels in vivo: a feasibility study," *Ultrasound Med. Biol.*, vol. 37, no. 6, pp. 980–995, Jun. 2011.

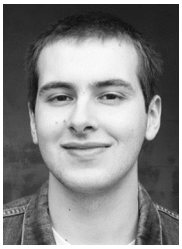

Clement Papadacci was born in February 1988 in Paris, France. He received a Magistere degree in fundamental physics and an M.S. degree in acoustics from Paris VII University in 2011. He is currently a Ph.D. student at the Institut Langevin in Paris, in the team Wave Physics for Medicine. His current research interests include ultrafast elasticity and anisotropy imaging of cardiovascular tissues.

Mathieu Pernot was born in November 1977 in St. Jean de Maurienne, France. He received his M.S. degree in 2001 and his Ph.D. in physics in 2004 from the University Paris VII. He is currently a researcher of the French National Institute of Health and Medical Research (INSERM) at the Langevin Institute in Paris, France. His current research interests include ultrasound imaging, shear wave elasticity imaging, wave focusing in heterogeneous media, and medical ultrasound therapy. He has been granted 12 patents in the field of ultrasonic therapy and published more than 40 papers in international peer-reviewed journals.

Mathieu Couade was born in February 1983 in Villecresnes, France. He received the Diplôme d'ingénieur in physics from the Ecole Supérieure de Physique et de Chimie Industrielles de Paris (ESPCI), and an M.S. degree and a Ph.D. degree in acoustics from Paris VII University in 2007 and 2011, respectively. He is currently in charge of the R&D of shear wave elastography for the company Supersonic Imagine in Aix en Provence, France. His research interests are in the medical applications of ultrasound. His main current research activities are focused on shear wave elastography and cardiovascular imaging.

Mathias Fink received the M.S. degree in mathematics from Paris University, France, in 1967 and the Ph.D. degree in solid-state physics in 1970. He then moved into medical imaging and received the Doctorat es-Sciences degree in 1978 from Paris University in the area of ultrasonic focusing with transducer arrays for real-time medical imaging. Dr. Fink is a professor of physics at the Ecole Supérieure de Physique et de Chimie Industrielles de la Ville de Paris (ESPCI), Paris, France, and at Paris VII University (Denis Diderot), France. In 1990, he founded the Laboratoire Ondes et Acoustique at ESPCI. In 2002, he was elected to the French Academy of Engineering and in 2003 to the French Academy of Science.

His current research interests include medical ultrasonic imaging; ultrasonic therapy; nondestructive testing; underwater acoustics; telecommunications; seismology; active control of sound and vibration; analogies between optics, quantum mechanics, and acoustics; wave coherence in multiply scattering media; and time reversal in physics. He has developed different techniques in acoustic imaging (transient elastography), wave focusing in inhomogeneous media (time-reversal mirrors), speckle reduction, and in ultrasonic laser generation. He holds 40 patents and he has published more than 300 articles.

Mickaël Tanter is a Research Professor of the French National Institute for Health and Medical Research (INSERM). For eight years, he has headed the Inserm laboratory U979, Wave Physics for Medicine, at the Langevin Institute, ESPCI Paris, France.

His main activities are centered on the development of new approaches in wave physics for medical imaging and therapy. His current research interests a wide range of topics: elastography using supersonic shear wave imaging, ultrafast ultrasound imaging, HIFU, and, more recently, the concept of fUtrasound (functional ultrasonic imaging of brain activity). He is the recipient of 24 world patents in the field of ultrasound and the author of more than 160 peer-reviewed papers and book chapters.

He is an Associate Editor of the *IEEE Transactions on Ultrasonics, Ferroelectrics, and Frequency Control*, and a member of the technical program committee of the IEEE International Ultrasonics Symposium and the administrative committee of the IEEE UFFC Society. In 2006, he co-founded Supersonic Imagine with M. Fink, J. Souquet, and C. Cohen-Bacrie. Supersonic Imagine is an innovative French company positioned in the field of medical ultrasound imaging and therapy; in 2009, the company launched a revolutionary ultrafast ultrasound imaging platform, called Aixplorer, with a unique real-time shear wave imaging modality for cancer diagnosis. Supersonic Imagine has more than 120 employees, 102 M€ venture capital, and has already sold more than 750 ultrasound systems worldwide. He has received ten scientific awards, including the Frederic Lizzi Early Career Award of the International Society of Therapeutic Ultrasound, the Montgolfier Prize of the French National Society for Industry Valorization, the Leon Brillouin Prize of the Institute of Electrical and Electronics Engineers (IEEE) and SEE society, the Yves Rocard prize of the French Society of Physics (SFP), the Sylvia Sorkin Greenfield Award of the American Association of Physicists in Medicine for the best paper published in Medical Physics in 2011, the Grand Prize of Medicine and Medical Research of the City of Paris, and the honored lecture of the Radiology Society of North America in 2012. He was recently awarded a prestigious European Research Council (ERC) Advanced Grant to develop fUltrasound applications.